Influence of strain and chemical substitution on the magnetic anisotropy of antiferromagnetic Cr_2O_3: An ab-initio study

Sai Mu and K. D. Belashchenko

Influence of strain and chemical substitution on the magnetic anisotropy of antiferromagnetic Cr_2O_3: an *ab-initio* study

Sai Mu[1, *] and K. D. Belashchenko[1]

[1]*Department of Physics and Astronomy and Nebraska Center for Materials and Nanoscience, University of Nebraska-Lincoln, Lincoln, Nebraska 68588, USA*

The influence of the mechanical strain and chemical substitution on the magnetic anisotropy energy (MAE) of Cr_2O_3 is studied using first-principles calculations. Dzyaloshinskii-Moriya interaction contributes substantially to MAE by inducing spin canting when the antiferromagnetic order parameter is not aligned with the hexagonal axis. Nearly cubic crystal field results in a very small MAE in pure Cr_2O_3 at zero strain, which is incorrectly predicted to be negative (in-plane) on account of spin canting. The MAE is strongly modified by epitaxial strain, which tunes the crystal-field splitting of the t_{2g} triplet. The contribution from magnetic dipolar interaction is very small at any strain. The effects of cation (Al, Ti, V, Co, Fe, Nb, Zr, Mo) and anion (B) substitutions on MAE are examined. Al increases MAE thanks to the local lattice deformation. In contrast, the electronic configuration of V and Nb strongly promotes easy-plane anisotropy, while other transition-metal dopants have only a moderate effect on MAE. Substitution of oxygen by boron, which has been reported to increase the Néel temperature, has a weak effect on MAE, whose sign depends on the charge state of B. The electric field applied along the (0001) axis has a weak second-order effect on the MAE.

I. INTRODUCTION

Cr_2O_3 is used as the active magnetoelectric material in voltage-controlled exchange bias devices which are attractive for magnetic memory and logic applications [1–7] due to their nonvolatility and low power consumption. The magnetic anisotropy energy (MAE) is a key parameter for such applications, which affects the thermal stability of the stored information and the coercivity of the antiferromagnet, which, in turn, controls the exchange bias, switching voltage, and switching speed. It also controls the domain wall width, which is important for domain-wall-mediated memory cells [6].

The easy-axis MAE of pure Cr_2O_3 is very small: 2×10^5 erg/cm³ (6 µeV/f.u.) at low temperatures [8]. The trade-off between conflicting device requirements makes it desirable to have the ability to tune MAE in both directions. Here we explore the MAE of Cr_2O_3 using first-principles calculations and investigate its response to epitaxial strain, chemical substitution, and applied electric field. The paper is organized as follows. Section II describes the computational methods. In Sec. III, the MAE of bulk Cr_2O_3 is evaluated, and different contributions are analyzed. The strain dependence of MAE in pure Cr_2O_3 is studied in Sec. IV. The effects of substitutional doping on both cation and anion site on MAE are explored in Sec. V. Conclusions are drawn in Sec. VIII.

II. COMPUTATIONAL DETAILS

The dominant contribution to MAE in Cr_2O_3 comes from the magnetocrystalline anisotropy (MCA), which is induced by spin-orbit coupling. MCA is calculated as the difference in the total energies for two orientations of the antiferromagnetic (AFM) order parameter $\mathbf{L}$: in the (0001) plane and along the hexagonal axis (see Fig. 1). Positive MCA corresponds to easy-axis anisotropy, i.e., $\mathbf{L}$ aligned with the hexagonal axis in the ground state.

First-principles calculations were performed using the projector augmented wave method (PAW) [10] implemented in the Vienna *ab-initio* simulation package (VASP) [11, 12]. The PAW pseudopotentials for the host elements correspond to the valence-electron configuration $4s^1 3d^5$ for Cr and $2s^2 2p^4$ for O. The exchange-correlation functional is treated in the local density approximation (LDA) [13]. The Coulomb correlations within the $3d$ shells of the transition-metal ions were described using the spherically averaged LDA+U method [14]. In this scheme, the Hamiltonian depends only on $U_{\text{eff}} = U - J$. For Cr atoms we used $U = 4.0$ eV and $J = 0.6$ eV ($U - J = 3.4$ eV), which give a good description of the electronic structure and magnetic properties [15]. The plane wave cutoff energy was set to 520 eV, and a Γ-centered Monkhorst-Pack k-point grid [16] was used for the Brillouin zone integration. The Hellmann-Feynman forces were converged to 0.005 eV/Å. MCA in bulk Cr_2O_3 was computed using the rhombohedral primitive cell (see Fig. 1) and the tetrahedral method based on the $8 \times 8 \times 8$ Γ-centered k-point mesh. A demanding energy criterion, 10^{-8} eV per Cr site, was employed to converge the total energy in the MCA calculations.

In order to assess the effect of epitaxial strain on the MCA of pure Cr_2O_3, we constrained the in-plane lattice parameters of the hexagonal unit cell and relaxed both the c parameter and all internal degrees of freedom [17]. The MCA of strained Cr_2O_3 was then calculated using the corresponding optimized rhombohedral cell.

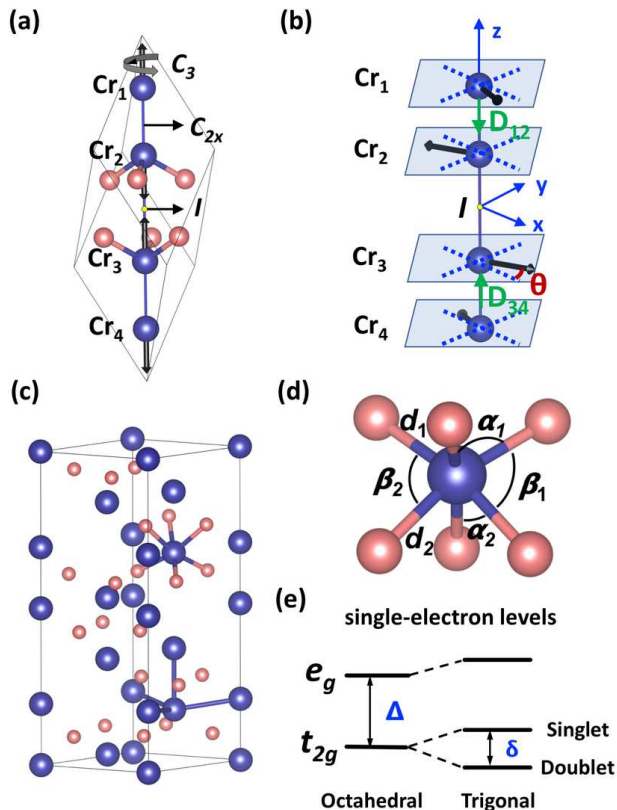To study the effects of alloying on MCA, we used a 30-atom hexagonal supercell (Fig. 1(c)) in which one Cr

FIG. 1. (a) Rhombohedral primitive and (c) hexagonal unit cell of Cr_2O_3. Blue (red) spheres denote Cr (O) atoms. Here we denote the 3-fold rotation axis (rhombohedral axis or hexagonal axis) as the z axis. The symmetry operations of paramagnetic Cr_2O_3 (inversion center I, 3-fold rotation axis C_3, and 2-fold rotation C_{2x}) are labeled in panel (a). Black arrows attached to Cr atoms denote their spin orientations. (b) Spin canting arising when the primary AFM order parameter $\mathbf{L}$ is along the x axis. Green arrows show the DMI vectors. (d) Local environment of the Cr atom showing bond angles and lengths. (e) Single-electron energy levels and crystal-field splitting parameters (Δ, δ). Structure visualization is done using VESTA [9].

or O atom was substituted by another defect atom. The tetrahedron method and the $4 \times 4 \times 2$ k-point mesh were used for Brillouin zone integration. For the substitution of Al, we also considered a larger 90-atom unit cell, for which a $2 \times 2 \times 2$ k-point mesh was employed.

Substitution of one atom in a given unit cell lowers the symmetry, while the random solid solution retains the symmetry of the parent lattice. Therefore, for each orientation of $\mathbf{L}$, it is necessary to average the energy over several supercells obtained by applying the point group symmetry operations of the original substituted site. Equivalently, one can use the same supercell but apply those symmetry operations to the *spin* configuration. We use the latter procedure to evaluate MCA for all substitutions in Cr_2O_3.

The electric field control of anisotropy in ferromagnetic

thin films has been widely studied [18–20], and the influence of electric field on the magnetic anisotropy of Cr_2O_3 clusters embedded in MgO was also discussed [21]. Here, we consider the effect of electric field on the MCA of bulk Cr_2O_3. The ionic displacements in the presence of electric field are evaluated using the method of Ref. 22, and the electronic contribution to MCA is included by evaluating the electrical enthalpy [23]. A similar analysis has been applied in the study of the magnetoelectric effect [24].

III. MAGNETOCRYSTALLINE ANISOTROPY OF PURE BULK Cr_2O_3

A. The role of Dzyaloshinskii-Moriya interaction

MAE corresponds to the total energy difference between spin configurations corresponding to in-plane and out-of-plane orientations of $\mathbf{L}$. For the out-of-plane orientation, the magnetic group has a C_3 axis passing through Cr sites, and the spin configuration is strictly collinear. However, for any other orientation, including in-plane, the Cr spins can tilt thanks to the Dzyaloshinskii-Moriya interaction (DMI) [25, 26].

We use the labeling of the Cr spins in the primitive cell shown in Fig. 1a. According to Moriya's rule [26], the DMI vector $\mathbf{D}_{12}$ for the pair of nearest-neighbor Cr atoms points along the hexagonal axis, as shown in Fig. 1b. For the spin pairs connected by the inversion center, such as atoms 2 and 3 in Fig. 1b, the DMI vector vanishes.

The primary order parameter in Cr_2O_3 is $\mathbf{L} = \boldsymbol{\mu}_1 - \boldsymbol{\mu}_2 + \boldsymbol{\mu}_3 - \boldsymbol{\mu}_4$, where the Cr sites are labeled as shown in Fig. 1a. The $R\bar{3}c$ space group allows the free energy invariant $L_x L'_y - L_y L'_x$, where $\mathbf{L}' = \boldsymbol{\mu}_1 + \boldsymbol{\mu}_2 - \boldsymbol{\mu}_3 - \boldsymbol{\mu}_4$ [27]. Microscopically, this invariant is generated by DMI and has a contribution from the nearest-neighbor Cr pairs. Clearly, if the primary $\mathbf{L}$ has a finite in-plane component, an orthogonal component of $\mathbf{L}'$ is induced as a secondary order parameter, resulting in the canting of the spins away from collinearity, as shown in Fig. 1b. This effect is similar to weak ferromagnetism generated by another invariant $L''_x M_y - L''_y M_x$, where $\mathbf{L}'' = \boldsymbol{\mu}_1 - \boldsymbol{\mu}_2 - \boldsymbol{\mu}_3 + \boldsymbol{\mu}_4$ is the primary order parameter in hematite [27]. Note that the relations $\boldsymbol{\mu}_1 = -\boldsymbol{\mu}_4$ and $\boldsymbol{\mu}_2 = -\boldsymbol{\mu}_3$ remain valid for an arbitrary orientation of $\mathbf{L}$.

The presence of spin canting according to the $\mathbf{L}'$ pattern is confirmed by explicit calculations allowing for spin non-collinearity when $\mathbf{L}$ lies in the (0001) plane. We found the induced transverse spin moments on Cr sites of about 0.09 μ_B, which amounts to a 1.7° canting angle.

Spin canting lowers the energy of the in-plane spin configuration and thereby reduces the MCA. To emphasize the role of this effect, in the following we discuss, in addition to the MCA energy K obtained with full (non-collinear) spin relaxation, the corresponding energy difference calculated while keeping the spin configuration collinear, denoted as K_{col}.

The experimental value of MCA in Cr_2O_3 is about 6 μeV/f.u. [8]. For pure, unstrained Cr_2O_3, with the theoretically optimized structure, we found $K_{col} = 2.5$ μeV/f.u. and $K = -44$ μeV/f.u. A similar value of $K = -52$ μeV/f.u. was obtained in the experimental structure [28]. Thus, the full calculation allowing for spin canting erroneously predicts easy-plane anisotropy. It is reasonable to attribute this error to the failure of the DFT+U calculation to give the correct deviation of the crystal-field splitting on Cr atoms from cubic. As we show below, a small change of about 30 meV in the crystal-field splitting is enough to make MCA positive. Despite this overall offset in MCA, we expect the trends in its variation under strain or substitution to be reasonably captured.

B. Analysis of the spin-orbit coupling energy

To gain insight into the origin of MCA, especially in the presence of an impurity, it is useful to consider the spin-orbit coupling energy for each atom, $E_{SO}(\mathbf{n}) = \sum_{\sigma\sigma'} \text{Tr}\, \xi_{\sigma\sigma'} \hat{\mathbf{L}} \cdot \hat{\mathbf{S}}_{\sigma\sigma'} \hat{\rho}_{\sigma'\sigma}(\mathbf{n})$, along with the individual terms in the summation over spin indices. Here the trace is over the orbital indices, $\xi_{\sigma\sigma'}$ is the l-diagonal spin-orbit coupling parameter, $\hat{\rho}(\mathbf{n})$ is the density matrix projected onto a local basis for a specific atom, calculated for $\mathbf{L} \parallel \mathbf{n}$, in the reference frame where the axis z is parallel to $\mathbf{n}$. Within second-order perturbation theory, $K \approx K_{SO} = [E_{SO}(\perp) - E_{SO}(\parallel)]/2$ [29], where the summation over all atoms is implied.

Table I lists the four contributions to the spin-orbit energy on one Cr site in Cr_2O_3, for two orientations of $\mathbf{L}$. We see that the diagonal majority-spin and the off-diagonal contributions to E_{SO} are comparable. On the other hand, the off-diagonal contribution dominates in the MCA as a result of spin canting. Table I also shows the that the small orbital moment on Cr comes largely from the majority-spin states.

TABLE I. Spin decomposition of the spin orbit energy $E_{SO}(\mathbf{n})$ (μeV), the orbital magnetic moment $M_l(\mathbf{n})$ (10^{-3} μ_B) on Cr, and their anisotropies. $\mathbf{n}$ is the orientation of the AFM order parameter.

	$\uparrow\uparrow$	$\downarrow\downarrow$	$\downarrow\uparrow$	$\uparrow\downarrow$	Total
$E_{SO}(\mathbf{z})$	-1012.91	-85.75	-1311.70	-1311.70	-3722.07
$E_{SO}(\mathbf{x})$	-1011.24	-87.13	-1334.62	-1334.62	-3767.61
K_{SO}	0.84	-0.69	-11.46	-11.46	-22.77
$M_l(\mathbf{z})$	41.80	-4.80			37.00
$M_l(\mathbf{x})$	41.93	-4.83			37.11
ΔM_l	-0.13	0.03			-0.11

IV. Cr_2O_3 UNDER EPITAXIAL STRAIN

Given that the crystal field in Cr_2O_3 is close to cubic, the MCA should be strongly affected by mechanical

strain. Here, we consider biaxial stress ($\sigma_{xx} = \sigma_{yy} = \sigma$, $\sigma_{zz} = 0$), which appears in a thin film that is laterally constrained by an epitaxial substrate. This is implemented by fixing the in-plane lattice parameter a and relaxing both c and the internal atomic positions. Figure 2 shows the dependence of MCA on the magnitude of epitaxial strain. In the linear region, K and K_{col} increase under tensile epitaxial strain at a rate of 61 and 44 μeV/f.u. per 1% of strain, respectively.
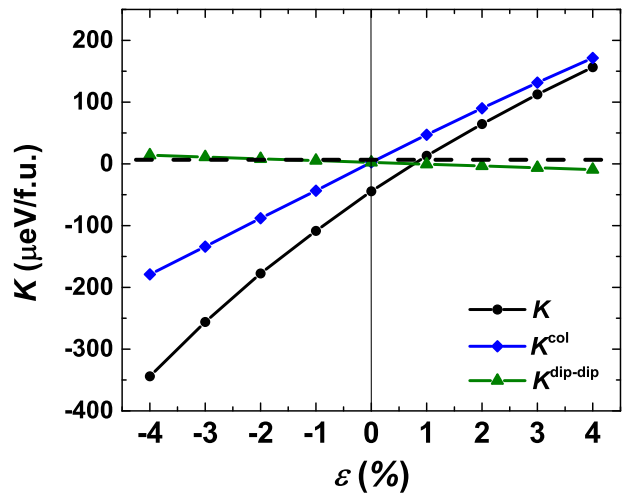

FIG. 2. Dependence of K (black circles) and K_{col} (blue diamonds) on the in-plane strain under biaxial stress in Cr_2O_3. Green triangles: dipole-dipole contribution to MAE. Dashed line: experimental MAE of unstrained Cr_2O_3.

The energy change due to spin canting (which accounts for the difference between K_{col} and K) can be written as $\Delta E(\theta) = -D\theta + \frac{1}{2}J\theta^2$, assuming small canting angle θ, where D and J are the effective DMI and exchange coupling parameters corresponding to the canting mode. The small contribution from the magnetic anisotropy is included in J. Minimization over θ gives the equilibrium values $\theta_0 = D/J$ and $\Delta E_0 = -\frac{1}{2}D^2/J$, where $\Delta E_0 = K - K^{col}$.

Figure 3 shows the parameters J, D, as well as the canting angle θ, as a function of epitaxial strain. Tensile strain ($\varepsilon > 0$) increases J while decreasing D, which results in the reduction of θ, which also decreases the difference between K and K^{col}, as seen in Fig. 2.

The increase of MCA under tensile strain is due to its effect on the crystal-field splitting δ of the t_{2g} states (Fig. 1d). This parameter is controlled by the O-Cr-O bond angles. There are two inequivalent angles, denoted α_1 and α_2 in Fig. 1d, with both O atoms belonging to the same crystallographic layer, and two (β_1 and β_2) with O atoms in different layers. Tensile strain increases the α_i angles while decreasing β_i, as seen in Table II, which also lists the bond lengths. Figure 4 also shows that the splitting of the t_{2g} states at the Γ point, which represents
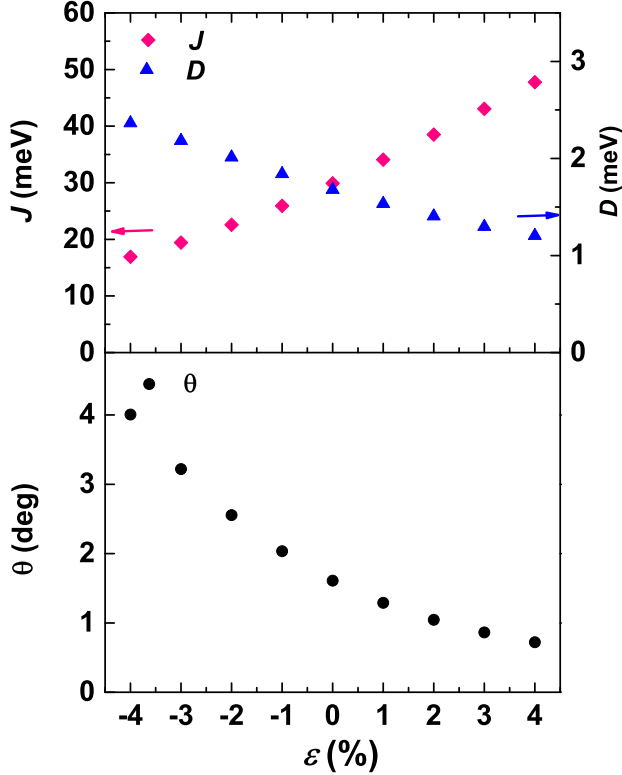
FIG. 3. (a) Effective exchange (J) and DMI parameters (D), and (b) the spin canting angle θ as a function of epitaxial strain.

FIG. 4. Epitaxial strain-dependent t_{2g} level splitting δ and the O-Cr-O bonding angle α_1.

the crystal-field parameter δ, decreases under increasing strain and passes through zero at a small positive value of ε.

The collinear approximation K_{col} exhibits the same trend as a function of strain as the full calculation K. To understand the origin of this trend, consider a localized independent-electron model of the Cr $3d$ shell. The Cr site symmetry C_3 splits the t_{2g} triplet into a doublet and a singlet separated by δ, which is typically less than 100 meV, while the energy of the e_g doublet Δ is of order 1 eV. As a basis set, we use linear combinations of cubic harmonics resulting from this splitting. In this basis, the crystal field Hamiltonian for the majority-spin $3d$ electrons is

$$H_{cf} = \begin{pmatrix} 0 & 0 & 0 & 0 & 0 \\ 0 & 0 & 0 & 0 & 0 \\ 0 & 0 & \delta & 0 & 0 \\ 0 & 0 & 0 & \Delta & 0 \\ 0 & 0 & 0 & 0 & \Delta \end{pmatrix}.$$

The full model Hamiltonian is obtained by adding the Hund exchange splitting $H_J = \epsilon \hat{\mathbf{S}} \mathbf{n}$ and spin-orbit coupling $H_{SO} = \xi \hat{\mathbf{l}} \hat{\mathbf{S}}$ to H_{cf}, $\mathbf{n}$ is the orientation of the order parameter $\mathbf{L}$, and the total energy is found as the sum of the lowest three eigenvalues. We emphasize that this
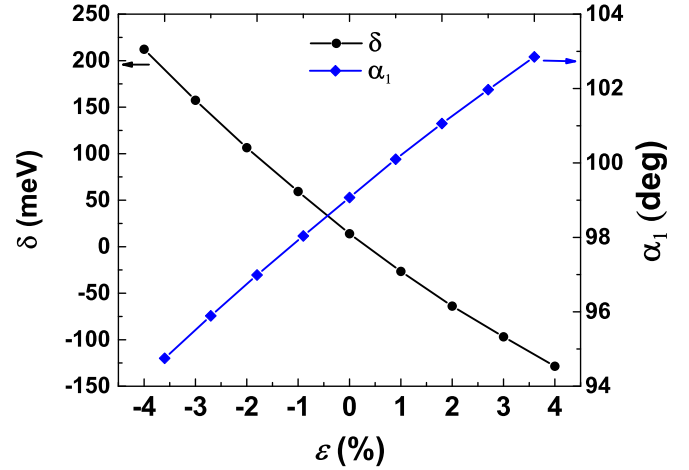
model neglects spin canting, and its results should be compared with K_{col}.

Figure 5 displays the dependence of K_{col} on the crystal-field parameters δ and Δ, at $\xi = 35$ meV and $\epsilon = 5$ eV. Clearly, positive or negative δ (i.e., singlet above or below the doublet) leads, respectively, to easy-plane or easy-axis anisotropy. Zero δ corresponds to cubic crystal field, for which $K_{col} = 0$, and the magnitude of K_{col} is proportional to δ (as long as $\delta \ll \Delta$). On the other hand, K_{col} depends inversely on Δ, tending to zero at $\Delta \to \infty$. These features are consistent with the first-principles results for the strain dependence of K_{col} shown above in Fig. 2: δ becomes more negative under tensile strain, and thereby K_{col} increases.
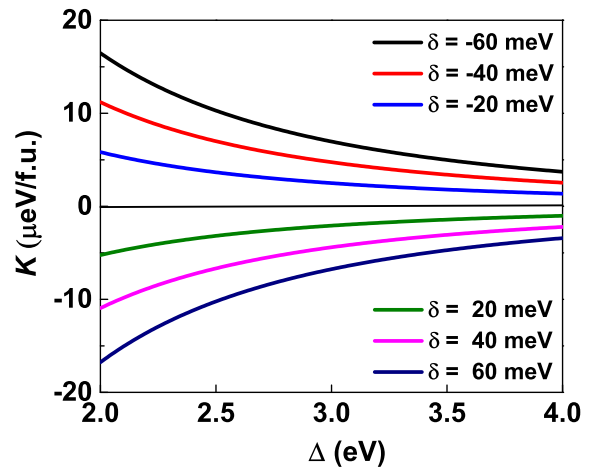

FIG. 5. Single electron model: MCA as a function of Δ, at $\xi = 35$ meV, for several values of δ. The Hund exchange parameter is set to 5 eV.

TABLE II. Cr-O bond length d_i (Å) in Cr_2O_3 under epitaxial strain ε or with Al substitution x. $\alpha_{1,2}$, $\beta_{1,2}$: O-X-O bond angles (deg) shown in Fig. 1. Lattice parameters (Å) and the c/a ratio are also given.

ε (%)	−4%	−3%	−2%	−1%	0%	+1%	+2%	+3%	+4%	$x = 2.8\%$		x=0.083	
Ligand	Cr−O	Cr−O	Cr−O	Cr−O	Cr−O	Cr−O	Cr−O	Cr−O	Cr−O	Cr^{NN}−O	Cr^{NNN}−O	Cr^{NN}−O	Cr^{NNN}−O
d_1	1.929	1.937	1.944	1.952	1.960	1.969	1.979	1.989	1.999	1.961	1.957	1.958	1.951
d_2	1.991	1.995	1.998	2.002	2.010	2.010	2.014	2.018	2.022	1.998	2.008	1.995	2.015
α_1	94.75	95.89	96.99	98.04	99.07	100.10	101.06	101.97	102.85	98.61	101.12	99.23	102.07
α_2	79.76	80.11	80.48	80.85	81.23	81.63	82.02	82.41	82.81	79.07	81.17	79.15	82.48
β_1	90.54	89.59	88.67	87.77	86.87	85.96	85.09	84.25	83.42	87.78	86.41	87.39	82.86
β_2	94.12	93.45	92.78	92.13	91.47	90.83	90.21	89.60	89.01	93.02	91.12	92.60	90.97
a	4.7470	4.7964	4.8459	4.8953	4.9440	4.9942	5.0437	5.0931	5.1426	4.2753		4.9260	
c/a	2.9776	2.9166	2.8570	2.7992	2.8570	2.6851	2.6307	2.5781	2.5267	2.7401		2.7413	

V. EFFECTS OF SUBSTITUTIONAL ALLOYING

Alloying can influence MCA through lattice deformations around the impurities, which affect the crystal-field splitting on the nearby Cr atoms. In addition, substitution of other transition-metal elements for Cr can result in a different electronic configuration on the impurity atoms, potentially leading to large contributions to MCA from spin-orbit coupling on those atoms.

Alloying can be introduced deliberately to tune MCA or other properties. For example, antiferromagnetic resonance measurements [30] on $(Cr_{1-x}Al_x)_2O_3$ single crystals revealed an enhancement of MAE by Al substitution. The magnetic properties of $(Cr_{1-x}Al_x)_2O_3$ thin films have also been explored [31]. Substitution of B for O can be used to increase the Néel temperature of Cr_2O_3 [32, 33] to facilitate room-temperature applications. On the other hand, Cr_2O_3 films for exchange-bias heterostructures are often grown on V_2O_3 [7], TiO_2 [34], Fe_2O_3 [35, 36], or Co [37] substrates, which can result in some degree of interfacial intermixing.

The effect of Al substitution on MCA is investigated in Sec. V A, and that of selected 3d and 4d transition-metal elements in Sec. V B; the role of boron substitution is studied in Sec. V C.

A. Al substitution

We considered substitution of one Cr atom by Al in a conventional 30-atom hexagonal supercell and in an enlarged 90-atom supercell with $\sqrt{3}\times\sqrt{3}$ translations in the ab plane. This amounts to 8.3 % and 2.8 % Al substitution, respectively. Figure 6a shows the calculated MCA for these two supercells, which is seen to increase at a rate of about 1.7 μeV/f.u. per 1% of Al substitution. Experimental measurement suggests the increase of about 0.7 μeV/f.u. per 1% of Al substitution [30]. Thus, the trend is predicted correctly, but the effect is overestimated.

The isovalent Al^{3+} cation has no 3d electrons and retains the C_3 symmetry of the Al site. The impurity induces a structural deformation of the surrounding lattice. Because Al atoms are smaller than Cr, the volume of the
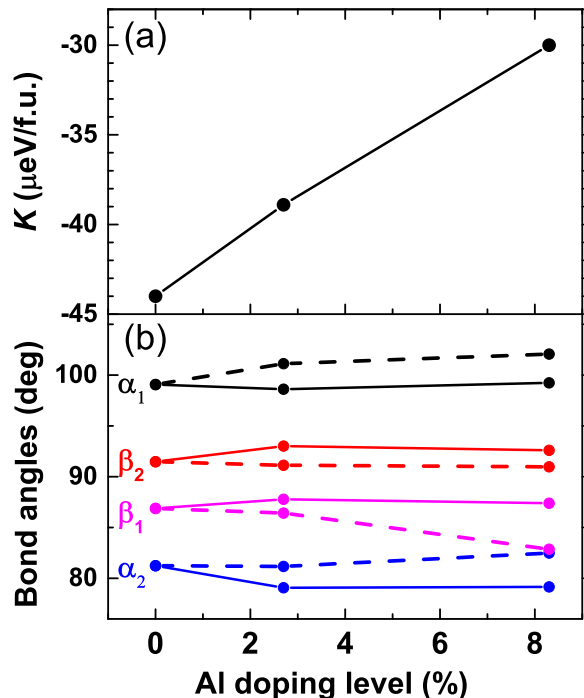

FIG. 6. Effect of Al doping on (a) K and (b) O-Cr-O bond angles defined in Fig. 1. Solid and dashed lines in panel (b) correspond to Cr atoms that are, respectively, first and second-nearest neighbors of Al. For the latter, the angles are averaged over the triplets of bonds that are equivalent in pure Cr_2O_3.

supercell decreases by about 0.13% per 1% Al doping, while the c/a ratio is almost unchanged (see Table II). This *homogeneous* strain is too weak to have an appreciable effect on MCA.

Figure 7 shows the site-resolved K_{SO}, which was defined in Sec. III B, for the Cr sites arranged in the order of increasing shortest distance from the Al impurity. The largest contribution to the enhancement of MCA comes from the three Cr atoms that are second-nearest neighbors of Al. This enhancement is induced by the lattice deformation around the Al impurity, which effectively
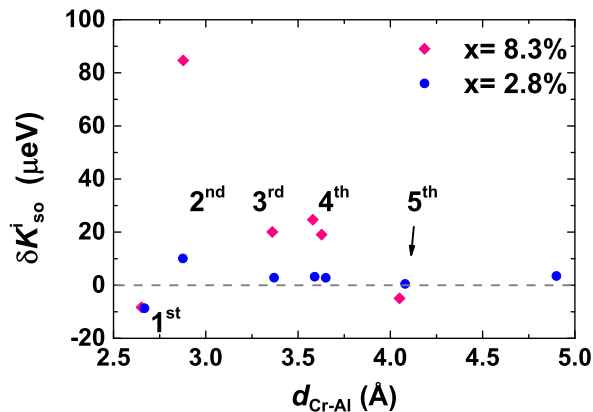
FIG. 7. The changes of atom-resolved anisotropies of the spin-orbit energies on one Cr site (meV) as a function of distance from Al to Cr(denoted as d_{Cr-Al}, from 1st nearest shell to 5th nearest shell), for Al doping level x is 2.8% and 8.3%. Zero point (dashed line) corresponds to the bulk value. Note that each point is an average over Cr atoms within a certain neighboring shell.

tunes the crystal field splitting on Cr.

The bond angles for the first and second-nearest Cr neighbors of Al are listed in Table II and shown in Fig. 6b. Due to the smaller size of Al compared to Cr, the O atoms shift toward it. As a result, the bond angles α_i increase for the second-nearest Cr (which is in the same buckled honeycomb layer with Al) and decrease for the first-nearest Cr (which is in a different layer). The changes of the β_i angles are opposite to those of α_i. The structural deformation is, thus, similar to tensile epitaxial strain on the second-nearest Cr atoms and compressive on the first-nearest one (see Table II). The changes in K_{SO} on these atoms are thus attributable to crystal-field effects that were discussed above.

B. Substitution of $3d$ and $4d$ elements for Cr

In this section, we consider the effects of Cr substitution by $3d$ (Ti, V, Fe, Co, Ni) and $4d$ (Nb, Mo, W) elements, replacing one Cr atom by an impurity in the 30-atom hexagonal cell. In order to obtain an accurate electron structure and MCA for doped Cr_2O_3, we used the *ab-initio* linear response method [38] to evaluate the U_{eff} parameters for the $3d$ impurities. For the $4d$ elements the U_{eff} parameters were obtained using the constrained occupation approach within the full-potential linear augmented plane-wave method [15, 39]. These values of U_{eff} are listed in Table III.

The results of MCA calculations are listed in Table III. The most striking effect on MCA comes from V and Nb doping: K is reduced at a rate of 216 or 156 μeV/f.u. per 1% substitution of V or Nb, respectively. This strong effect is not attributable to lattice distortion, which we ex-

plicitly rule out by recalculating the MCA of pure Cr_2O_3 in the distorted geometry for the given substitution (denoted as $K^\dagger$ in Table III). We see that $K^\dagger$ for V and Nb-substituted structures is close to the value of K for pure Cr_2O_3. Further, the large negative MCA in V and Nb-substituted systems is almost entirely due to the large negative K_{SO} on the impurity atom, and it occurs in the collinear approximation as well (see the K_{col} values in Table III). Therefore, to understand the strong effect of V and Nb on MCA, we focus on K_{col}.

Both V^{3+} and Nb^{3+} are $3d^2$ ions. Repeating the calculations of MCA for the simple model described in Sec. IV, but with either 1 or 2 electrons in the $3d$ shell instead of 3, we find a very large MCA that strongly depends on the t_{2g} splitting parameter δ (see Fig. 8).
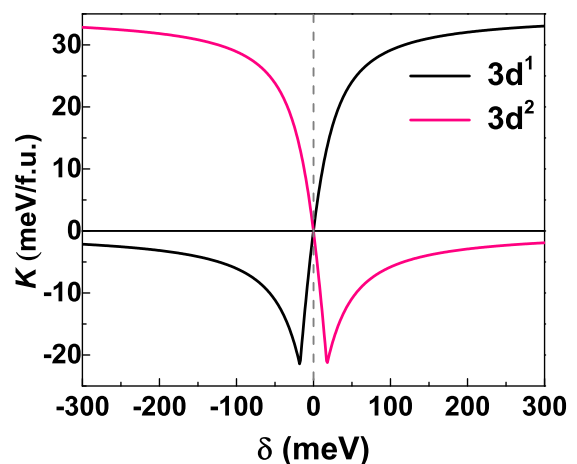

FIG. 8. MCA as a function of the t_{2g} crystal-field parameter δ, at $\xi = 35$ meV, for $3d^1$ and $3d^2$ configurations. Note the different scale (meV) for MCA compared to Fig. 5.

The mechanism of MCA can be understood as follows. The singlet has character $m = 0$ and the doublet $m = \pm1, \pm2$ (in the hexagonal frame). For $\mathbf{L} \parallel \hat{z}$, the spin-orbit coupling linearly splits the doublet without affecting the singlet. The upper branch of the split doublet crosses the singlet state at $\xi = 2\delta$. For $\mathbf{L} \perp \hat{z}$, the singlet is mixed with the doublet, also splitting the latter, and there are no level crossings.

For the $3d^2$ configuration, at $\delta > 2\xi$ the spin-orbit coupling only reduces the energy of the in-plane spin configuration. This reduction is inversely proportional to δ and corresponds to the behavior of K at large δ in Fig. 8. Once δ is reduced down to 2ξ, the level crossing leads to an abrupt switch to a linear region in $K(\delta)$. At $\delta = 0$ the crystal field is cubic and, therefore, K vanishes. At negative δ, K continues to rise and approaches a large positive value at $|\delta| \gg \xi$. In this limit, only the splitting of the doublet at $\mathbf{L} \parallel \hat{z}$ is important. Since this doublet is half-filled, there is a large energy gain for $\mathbf{L} \parallel \hat{z}$, leading to a large easy-axis anisotropy.

TABLE III. Properties of Cr_2O_3 with a substitution of one Cr atom by a dopant X in a 30-atom supercell (8.3% substitution). d_1, d_2: X-O bond lengths (Å); $\alpha_{1,2}$, $\beta_{1,2}$: O-X-O bond angles (deg) shown in Fig. 1; U, J, U_{eff}: effective interaction parameters (eV) for the atom X; K (μeV/f.u.): MCA with full spin relaxation; K_{col} (μeV/f.u.): MCA obtained assuming collinear spin states; $K^\dagger$ and $K^\dagger_{col}$ (μeV/f.u.): same as K and K_{col} but with X replaced back by Cr with the structure optimized in the presence of X; K_{SO}^X (μeV): see Sec. III B; μ_X (μ_B): local magnetic moment on the defect atom X; η (μeV/f.u.): rate of change of K per 1% substitution of Cr by X. Bond lengths and angles are not listed for Jahn-Teller elements Ti, Ni, and Zr.

X	Cr	Ti	V	Fe	Co	Ni	Zr	Nb	Mo
d_1	1.96	–	1.976	1.937	1.898	–	–	2.058	2.100
d_2	2.01	–	2.046	2.061	1.918			2.126	2.062
α_1	99.07	–	100.2	101.47	98.21	–	–	99.62	98.48
α_2	81.23	–	79.68	78.97	82.97	–	–	77.95	80.53
β_1	86.87	–	86.88	86.44	86.78	–	–	88.13	87.42
β_2	91.47	–	91.31	90.89	91.07	–	–	92.36	92.27
c	13.553	13.609	13.580	13.555	13.489	13.502	13.711	13.747	13.669
a	4.945	4.949	4.949	4.944	4.920	4.933	4.997	4.964	4.963
c/a	2.741	2.750	2.744	2.742	2.742	2.737	2.744	2.770	2.754
U	4.0	3.95	4.24	5.35	5.89	6.54	1.73	2.21	3.16
J	0.58	0.47	0.54	0.75	0.81	0.85	0.70	0.55	0.53
U_{eff}	3.4	3.5	3.7	4.6	5.1	5.7	1.0	1.7	2.6
μ_X	2.91	0.82	1.92	4.24	0.04	1.07	0.04	1.20	2.40
$K^\dagger$ $(K^\dagger_{col})$	–	−42 (−1.4)	−47 (1.7)	−38 (8)	−35 (1.7)	−41 (4.4)	−33 (9)	−43 (−20)	−64 (−10)
K (K_{col})	−44 (2.5)	−98 (−79)	−1820 (−1240)	−53 (−1.7)	−15 (10)	−56 (−13)	2 (15)	−1360 (−1350)	−66 (−50)
K_{SO}^X	−24	−380	−5560	−85	−48	−63	−3	−5980	−306
η	0	−6.5	−213	−1.1	3.5	−1.4	5.5	−159	−2.6

The situation for the $3d^1$ configuration at splitting δ is almost identical to $3d^2$ at $-\delta$; the tiny difference, which is unnoticeable in Fig. 8, comes only from the mixing with higher-lying states.

This fully localized ionic model neglects hybridization, which should considerably reduce the anisotropy and smear out the cusps at $|\delta| = 2\xi$. However, strong negative MCA for the $3d^2$ impurities V and Nb is consistent with the prediction of this model for $\delta > 0$.

Further, the $3d^2$ configuration at $\delta < 0$ and the $3d^1$ configuration at $\delta > 0$ are degenerate in the absence of spin-orbit coupling and are, therefore, expected to undergo Jahn-Teller distortion. In contrast, $3d^2$ at $\delta > 0$ and $3d^1$ at $\delta < 0$ are not subject to the Jahn-Teller effect. The fact that $3d^2$ impurities V and Nb in Cr_2O_3 don't, while $3d^1$ impurities Ti and Zr do, experience Jahn-Teller distortion [32] is consistent with δ being positive for all these dopants and with the finding of large and negative K for V and Nb. On the other hand, the distortion strongly changes the crystal field for Ti and Zr, invalidating the prediction of large positive MCA for the $3d^1$ configuration (Fig. 8). As seen in Table III, Zr (Ti) increases (reduces) K at a rate of 5.9 μeV/f.u. (6.5 μeV/f.u.) per 1% substitution. For both Ti and Zr, the value of $K^\dagger$, which is obtained by replacing the impurity back by Cr while maintaining the deformed structure, is similar to ideal Cr_2O_3. This indicates that the effect of Ti and Zr on MCA comes from the impurity atom itself.

Consistent with the above analysis, V and Nb atoms carry large orbital moments for the in-plane spin configuration (-0.78 and -0.33 μ_B, respectively), but not for out-of-plane configuration (-0.04 and -0.06 μ_B). (The negative signs indicate that orbital and spin moments

are antiparallel.) Further, if one electron is added to the V-doped Cr_2O_3 supercell by introducing a homogeneous positive background charge, V^{3+} turns into V^{2+} with a $3d^3$ configuration. This system has an MCA of -3.3 μeV/f.u., which is larger than bulk Cr_2O_3. This confirms that the large negative MCA results only from V^{3+} and Nb^{3+} ions in the $3d^2$ electronic configuration.

As seen in Table III, K and K_{col} are almost the same for Nb, while there is a large difference for V, which comes from the spin canting in the in-plane spin configuration. The canting angle for Nb is only 0.4°, while for V it is as large as 2.2°.

In addition to Ti and Zr, the Ni impurity with the low-spin $3d^7$ configuration also experiences a Jahn-Teller distortion, which originates in the single occupation of the degenerate e_g orbitals [32], while the t_{2g} states are filled for both spins channels. Ni substitution has a very small negative effect on MCA.

For isovalent Mo substitution, the reduction of $K^\dagger_{col}$ relative to pure Cr_2O_3 (from 2.5 to -10 μeV/f.u.) reflects the local strain effect, which primarily affects the second-nearest Cr neighbors of Mo (as follows from the analysis of K_{SO}). The substitution of Mo in the distorted structure further reduces MCA to -50 μeV/f.u. thanks to a large negative K_{SO} for the Mo atom. The contribution of spin canting to K is reduced in Mo-doped Cr_2O_3 due to the enhancement of the exchange interaction near the Mo atom. Overall, Mo reduces MCA at a small rate of 2.6 μeV/f.u. per 1% Mo substitution.

The exchange interaction in the Mo-doped case is noteworthy. The effect of alloying on the Néel temperature can be estimated from the values of the exchange energies E_i, which represent the energy cost to reverse the local
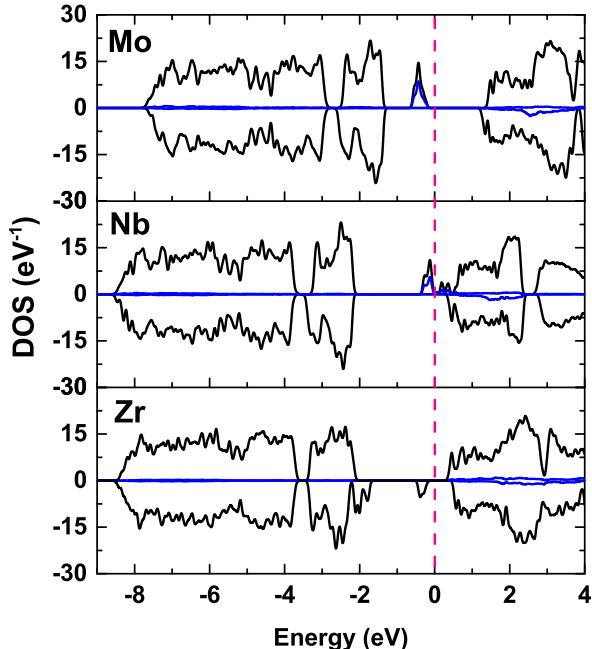
FIG. 9. Total density of states (DOS) of Zr, Nb and Mo doped Cr_2O_3, shown in black lines. The 4d impurity states are shown in blue lines. $\pm$ sign of DOS indicates different spin channels. The Fermi energy has been shifted to 0 eV.

moment on atom i [32]. In pure Cr_2O_3 this energy is 120 meV [32]. It is increased to 620 meV for the Mo dopant, 240 meV for its nearest Cr neighbors, and 420 meV for the second Cr neighbors of Mo. This enhancement can be attributed to the impurity state in the band gap (see Fig. 9), which mediates the exchange interaction. A rough estimate based on the mean-field approximation suggests that 1% Mo substitution increases the Néel temperature by about 8%, which is comparable to the effect of B substitution for O [32, 33].

The isovalent Co^{3+} impurity ($3d^6$ configuration) prefers the low-spin state with fully filled t_{2g} states and empty e_g states [32]. The spin moment on Co is only 0.04 μ_B. A somewhat enhanced $K^\dagger$ indicates that the pure structural relaxation effect increases the MCA, but an even larger enhancement comes from K_{SO} on Co. Overall, Co increases MCA by 3.6 μeV/f.u. per 1% substitution. The enhancement of MCA under Co doping may explain the observation [40] of an enhanced perpendicular anisotropy in Co/Cr_2O_3 bilayers.

Substitution of Cr by Fe slightly reduces K, which could be the origin of the reduced coercivity field in Cr_2O_3/Fe_2O_3 compared to Cr_2O_3/Pt [36].

For most practical applications, Cr_2O_3 alloyed with other elements should retain its insulating properties. Impurities of 3d transition metals introduce impurity levels inside the band gap [32], which are likely to degrade the insulating properties for sizable levels of substitution.

Therefore, transition-metal substitutions are likely to be useful only if they have a strong effect on MCA.

Our results suggests that MCA of Cr_2O_3 can be effectively reduced, or even switched to easy-plane, by a very small substitution of V or Nb on the order of 0.05%. The density of states for Nb-doped Cr_2O_3, as seen in Fig. 9, shows filled impurity states close to the bottom of the conduction band, which may act as electron donors. In contrast, the excitation gap in V-doped Cr_2O_3 is almost 2 eV wide, with filled impurity states close to the top of the valence band and empty impurity states close to the bottom of the conduction band [32]. This difference is due to a much larger on-site Coulomb interaction in the 3d shell of V. The lack of easily excitable impurity states in V-doped Cr_2O_3 makes V preferable to Nb as an alloying element if reduced MCA is desired. For Cr_2O_3 films grown on a V_2O_3 substrate [7], even a small Cr/V interdiffusion can strongly reduce MCA or turn it to easy-plane.

The strongest positive effect on MCA, among transition elements, is from Zr substitution, which is about 3 times more effective than Al. However, similar to Nb, Zr has shallow electron donor states (see Fig. 9), which are likely to degrade the insulating properties. Cobalt may be a preferable alternative: its effect on MCA is predicted to be twice stronger than Al, while the insulating properties may be expected to be preserved thanks to the wide excitation gap for the Co^{3+} ions in Cr_2O_3 [32].

C. Boron substitution for oxygen

Substitution of boron on the oxygen sublattice in Cr_2O_3, on the level of a few percent, was shown to considerably increase the Néel temperature [32, 33]. Given the potential utility of this material for applications, it is important to examine the effect of boron substitution on the magnetic anisotropy. We focus on the B^{2-} and B^{1-} charge states, which, according to theoretical calculations [32], are expected to enhance the Néel temperature.

The neutral B^{2-} impurity strongly distorts the local geometry [32]. As seen from Table IV, these impurities decrease MCA. The analysis of K_{SO} indicates this decrease is primarily due to the modified crystal field on the four Cr atoms that are bonded with B. Comparison of K and $K^\dagger$ shows that the states of B somewhat increase MCA relative to O, but this effect only partially compensates the reduction of MCA due to the structural distortion.

TABLE IV. K and related quantities (μeV/f.u.; see Table III for definitions) for Cr_2O_3 with 5.6% substitution of B for O. The spin structure for B^{3-} could not be converged.

MCA	bulk	B^{2-}	B^{1-}	B^{3-}
K (K_{col})	-44 (2.5)	-62 (-2.2)	26 (60)	— (-206)
$K^\dagger$ $(K^\dagger_{col})$	-44 (2.5)	-71 (-12)	-30 (14)	-80 (-21)

The B^{1-} charged state was enforced by introducing a

homogeneous background charge to the supercell. It is seen from Table IV that B^{1-} impurities increase MCA at a rate of $+8.4$ μeV/f.u. per 1% substitution. This increase is almost entirely due to the presence of B electronic states, because $K^{\dagger}$, which accounts for the structural distortion alone, is only slightly increased compared to pure Cr_2O_3. It originates from the four nearby Cr sites, as follows from the analysis of K_{SO}.

VI. MAGNETIC DIPOLAR INTERACTIONS

A calculation [28] based on the experimental structure for Cr_2O_3 estimated the contribution from the magnetic dipolar interaction to MAE at $K_{dd} = 3$ μeV/f.u. This value is comparable to and of the same sign as the experimental MCA. Here we study the effect of epitaxial strain on K_{dd}, using the theoretically optimized structures.

The interaction energy of two localized magnetic dipoles $\boldsymbol{\mu}_i$ and $\boldsymbol{\mu}_j$ separated by $\mathbf{r}_{ij} = \mathbf{r}_j - \mathbf{r}_i$ is

$$E_{ij} = -\frac{\mu_0}{4\pi}\frac{3(\boldsymbol{\mu}_i \cdot \mathbf{n}_{ij})(\boldsymbol{\mu}_j \cdot \mathbf{n}_{ij}) - \boldsymbol{\mu}_i \cdot \boldsymbol{\mu}_j}{r_{ij}^3}, \quad (1)$$

where $\mathbf{n}_{ij} = \mathbf{r}_{ij}/r_{ij}$. The sum over all pairs of dipoles gives the total magnetostatic energy. In the calculations for Cr_2O_3 we assumed $\mu_i = 3$ μ_B.

For the unstrained theoretical structure we found $K_{dd} = 2.4$ μeV/f.u., in good agreement with Ref. 28. The results as a function of epitaxial strain are shown in Fig. 2. We see that K_{dd} is only comparable to MCA in the unstressed system, and it has an opposite trend under strain.Thus, it does not materially affect the strain dependence of MAE.

VII. EFFECT OF ELECTRIC FIELD

Here we investigate the response of MCA to a uniform electric field applied along the rhombohedral axis. Figure 10 shows K and K^{col} in the presence of such field. The dependence is quadratic, and the response coefficient is similar for K and K^{col}: $K = -44.4 + 1.8E_z^2$ and $K_{col} = 2.5 + 1.7E^2$ (in units of μeV/f.u., with E_z in V/nm). The dependence is rather weak thanks to the rigidity of the crystal lattice. For example, a 1 V/nm electric field changes the Cr-O bond length by only about 1%. We found that the effect of the electric field on MCA is entirely due to the induced ionic displacements; the electronic contribution is negligible.

Although the effect of electric field on MCA is relatively weak, it could be used to switch the anisotropy from easy-plane to easy-axis by voltage in Cr_2O_3 that is doped (for example, by vanadium) slightly beyond the point where MCA vanishes. Such voltage control of magnetic anisotropy in an antiferromagnet could lead to interesting applications.
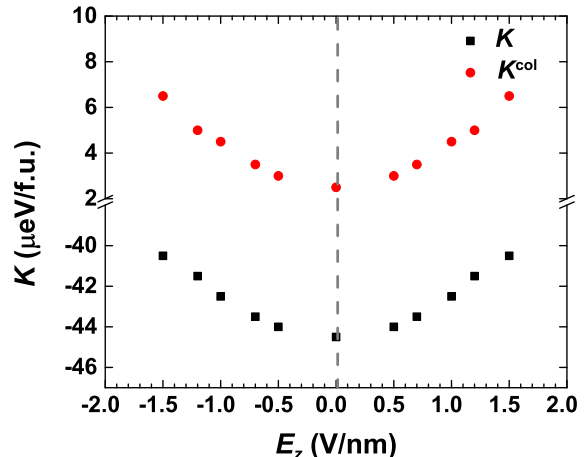

FIG. 10. Dependence of K and K^{col} on the electric field applied along the rhombohedral axis.

VIII. CONCLUSIONS

The influence of epitaxial strain, substitutional alloying, and electric field on the MAE of Cr_2O_3 has been studied using the DFT+U method. The MAE of pure, unstrained Cr_2O_3 is very small, because the crystal field of the Cr ion is close to cubic, and the calculations fail to reproduce the correct positive sign of MCA. Tensile epitaxial strain increases MCA at a rate of about 60 μeV/f.u. per 1% strain, which is due to the changing crystal-field splitting of the t_{2g} states. The large response of MCA makes strain an effective tuning parameter for applications.

Substitution of Cr by Al is predicted to increase MCA at the rate of 1.7 μeV/f.u. per 1% substitution, in qualitative agreement with experiment. This effect is mediated by the structural distortion around the Al impurities. Among the $3d$ and $4d$ transition-metal alloying elements, V and Nb have the strongest effect on MCA, reducing K at very large rates of about 220 and 160 μeV/f.u. per 1% substitution, respectively. This large effect is due to the partial $(3d^2)$ filling of the t_{2g} states, which enables strong in-plane anisotropy thanks to a spin-orbital selection rule. On the other hand, Co and Zr are predicted to increase MCA at a moderate rate that is 2-3 times larger than that of Al. For applications where the alloyed Cr_2O_3 needs to retain good insulating properties, V is the element of choice for reducing MAE or switching it to easy-plane, while Al or Co are preferred for increasing MAE.

Boron substitution for O increases the Néel temperature of Cr_2O_3 and is, therefore, desirable for applications. We predict that neutral B^{2-} impurities tend to moderately decrease MAE, while B^{1-} increase it considerably.

Magnetostatic contribution to MAE is estimated at 2.4 μeV/f.u. in unstrained Cr_2O_3, which is comparable to the

experimental MAE of 6 μeV/f.u. However, the magneto-static contribution remains small under epitaxial strain, while the magnetocrystalline anisotropy is strongly modified by it.

The electric field applied along the hexagonal axis is predicted to increase MCA quadratically ($K \sim E_z^2$). The field $E_z \sim 1$ V/nm increases MAE by about 1.8 μeV/f.u. If Cr_2O_3 is alloyed with V slightly beyond the point where MAE vanishes, the electric field could be used to switch MAE from easy-plane to easy-axis.

[1] C. Binek and B. Doudin, J. Phys. Condens. Matter **17**, L39 (2005).

[2] X. He, Y. Wang, N. Wu, A. N. Caruso, E. Vescovo, K. D. Belashchenko, P. A. Dowben, and C. Binek, Nat. Mater. **9**, 579 (2010).

[3] K. D. Belashchenko, Phys. Rev. Lett. **105**, 147204 (2010).

[4] T. Ashida, M. Oida, N. Shimomura, T. Nozaki, T. Shibata and M. Sahashi, Appl. Phys. Lett. **106**, 132407(2015) .

[5] K. Toyoki, Y. Shiratsuchi, A. Kobane, C. Mitsumata, Y. Kotani, T. Nakamura, and R. Nakatani, Appl. Phys. Lett. **106**, 162404 (2015).

[6] K. D. Belashchenko, O. Tchernyshyov, A. A. Kovalev and O. A. Tretiakov, Appl. Phys. Lett. **108**, 132403 (2016).

[7] T. Kosub, M. Kopte, R. Hühne, P. Appel, B. Shields, P. Maletinsky, R. Hübner, M. O. Liedke, J. Fassbender, O. G. Schmidt and D. Makarov, Nat. Commun. **8**, 13985 (2017).

[8] S. Foner, Phys. Rev. **130**, 183 (1963).

[9] K. Momma and F. Izumi, Crystallogr. Comput., IUCr Newslett., **7**, 106 (2006).

[10] P. E. Blöchl, Phys. Rev. B **50**, 17953 (1994).

[11] G. Kresse, J. Hafner, Phys. Rev. B **48**, 13115 (1993).

[12] G. Kresse, J. Furthmüller, Phys. Rev. B **54**, 11169 (1996).

[13] J. P. Perdew and A. Zunger, Phys. Rev. B. **23** (10), 5048 (1981).

[14] S. L. Dudarev, G. A. Botton, S. Y. Savrasov, C. J. Humphreys and A. P. Sutton, Phys. Rev. B **57**, 1505 (1998).

[15] S. Shi, A. L. Wysocki, K. D. Belashchenko, Phys. Rev. B **79**, 104404 (2009).

[16] H. Monkhorst and J. D. Pack, Phys. Rev. B **13**, 5188 (1976).

[17] S. Mu, Ph.D. thesis, *First Principles study of magneto-electric materials* (University of Nebraska-Lincoln, 2014).

[18] F. Ibrahim, H. X. Yang, A. Hallal, B. Dieny, and M. Chshiev, Phys. Rev. B **93**, 014429 (2016).

[19] P. V. Ong, N. Kioussis, P. Khalili Amiri and K. L. Wang, Sci. Rep. **6**, 29815 (2016).

[20] T. Maruyama, Y. Shiota, T. Nozaki, K. Ohta, N. Toda, M. Mizuguchi, A. A. Tulapurkar, T. Shinjo, M. Shiraishi, S. Mizukami, Y. Ando and Y. Suzuki, Nat. Nanotechnol. **4**, 158 (2009).

[21] D. Halley, N. Najjari, F. Godel, M. Hamieh, B. Doudin, and Y. Henry, Phys. Rev. B **91**, 214408 (2015).

[22] J. Iniguez, Phys. Rev. Lett. **101**, 117201 (2008).

[23] I. Souza, J. Iniguez, and D. Vanderbilt, Phys. Rev. Lett. **89**, 117602 (2002).

[24] S. Mu, A. L. Wysocki, K. D. Belashchenko, Phys. Rev. B **89**, 174413 (2014).

[25] I. Dzyaloshinskii, J. Phys. Chem. Solids **4**, 241(1958).

[26] T. Moriya, Phys. Rev. **120**, 91 (1960).

[27] A. S. Borovik-Romanov and H. Grimmer, International Tables for Crystallography (2006). Vol. D, Chapter 1.5, pp. 105-149.

[28] J. O. Artman, J. C. Murphy, S. Foner, Phys. Rev. **138**, A912 (1965).

[29] V. Antropov, L. Ke, D. Aberg, Solid State Communications **194**, 35 (2014).

[30] S. Foner, J. Appl. Phys **32**, S63 (1961).

[31] L. Fallarino, C. Binek, A. Berger, Phys. Rev. B **91**, 214403 (2015).

[32] S. Mu, A. L. Wysocki, K. D. Belashchenko, Phys. Rev. B **87**, 054435 (2013).

[33] M. Street, W. Echtenkamp, T. Komesu, S. Cao, P. A. Dowben, and C. Binek, Appl. Phys. Lett. **104**, 222402 (2014).

[34] W. Yuan, T. Su, Q. Song, W. Xing, Y. Chen, T. Wang, Z. Zhang, X. Ma,P. Gao, J. Shi and W. Han, Sci. Rep. **6**, 28397 (2016).

[35] I. Banerjee, H. Kim, D. Pisani, K. P. Mohanchandra, and G. P. Carman, J. Alloy Compd. **614** 305 (2014).

[36] N. Shimomura, S. P. Pati, T. Nozaki, T. Shibata, and M. Sahashi, AIP Adv. **7**, 025212 (2017).

[37] T. Nozaki, M Oida, T. Ashida, N. Shimomura, and M. Sahashi, Appl. Phys. Lett. **103**, 242418 (2013).

[38] M. Cococcioni and S. de Gironcoli, Phy. Rev B **71**, 035105 (2005).

[39] S. Blügel and G. Bihlmayer, in *Computational Nanoscience: Do It Yourself!* ed. by J. Grotendorst,

S. Blügel, and D. Marx, NIC Series Vol. 31, p. 85 (John von Neumann Institute for Computing, Jülich, 2006).

[40] Y. Shiratsuchi, H. Oikawa, S. Kawahara, Y. Takechi, T. Fujita and R. Nakatani, Appl. Phys. Express **5**, 043004 (2012).